11-2013

Calculation of Magnet Losses in Concentrated-Winding Permanent-Magnet Synchronous Machines Using a Computationally Efficient Finite-Element Method

Peng Zhang
Marquette University

Gennadi Y. Sizov
Marquette University

Jiangbiao He
Marquette University

Dan M. Ionel
University of Wisconsin - Milwaukee

Nabeel Demerdash
Marquette University, nabeel.demerdash@marquette.edu

IEEE Transactions on Industry Applications, Vol. 49, No. 6 (November-December 2013): 2524-2532. DOI.

Calculation of Magnet Losses in Concentrated-Winding Permanent-Magnet Synchronous Machines Using a Computationally Efficient Finite-Element Method

Peng Zhang
Department of Electrical and Computer Engineering, Marquette University, Milwaukee, WI
Gennadi Y. Sizov
Rockwell Automation, Mequon, WI
Jiangbiao He
Department of Electrical and Computer Engineering, Marquette University, Milwaukee, WI

Dan M. Ionel
Regal Beloit Corporation, Beloit, WI
Nabeel A. O. Demerdash
Department of Electrical and Computer Engineering, Marquette University, Milwaukee, WI

Abstract:

The proposed hybrid method combines computationally efficient finite-element analysis (CE-FEA) with a new analytical formulation for eddy-current losses in the permanent magnets (PMs) of sine-wave current-regulated brushless synchronous motors. The CE-FEA only employs a reduced set of magnetostatic solutions yielding substantial reductions in the computational time, as compared with the conventional FEA. The 3-D end effects and the effect of pulsewidth-modulation switching harmonics are incorporated in the analytical calculations. The algorithms are applied to two fractional-slot concentrated-winding interior PM motors with different circumferential and axial PM block segmentation arrangements. The method is validated against 2-D and 3-D time-stepping FEA.

SECTION I. Introduction

Over the last decade, brushless permanent-magnet (BLPM) motor technology was established as the preferred choice for high-efficiency applications [1]. In particular, the motors operated by sine-wave current-regulated vector-controlled power electronic drives, which are commonly referred to as permanent-magnet (PM) synchronous or sine-wave machines, are of great interest and are the topic of the current paper.

The latest generations of BLPM sine-wave motors employ rare-earth NdFeB PMs, which are electrically conductive and therefore prone to eddy-current losses. The satisfactory estimation of PM losses is very important not only for optimizing the design of high-efficiency motors but also for the growing number of machines dedicated to fault tolerant applications, in which local losses and heating are of particular concern. The PM losses can be particularly significant in BLPM motors that have a rich content of magnetomotive force (MMF) harmonics. This is the case for fractional-slot concentrated-winding topologies, which in turn are recommended due to their potential benefits for lower cost at specified performance and enhanced fault-handling capability. Two such interior PM (IPM) motors serve as case studies in this paper.

Calculation of rotor losses has been a common theme for different types of electrical machines, e.g., [2]–[3] [4] [5] [6]. Although time-stepping finite-element analysis (TS-FEA) has, in principle, the advantage of high accuracy, its applicability, particularly for optimization studies involving many candidate designs, is still limited due to the prohibitive requirements for computational resources. The presence of 3-D end effects further complicates the numerical problems, and hence, different analytical, and hybrid analytical, formulations combined with FEA algorithms have been proposed [7], [8]. The method introduced in this paper is of the later type, which is of particular interest as it leads to a satisfactory tradeoff between accuracy and computational speed.

Recently, the authors have proposed a technique for computationally efficient FEA (CE-FEA) [9]–[10] [11]. The method uses only a reduced set of magnetostatic field solutions in order to satisfactorily estimate sine-wave current-regulated BLPM motor performance. This paper brings further significant

contributions that enable the calculation of PM eddy-current losses based on magnetic FEA and on a theoretical development that includes the 3-D end effects. The pulsewidth-modulation (PWM) switching losses in the PMs are also quantified, together with the effect of various PM block segmentation techniques, on two IPM example motors of the 12-slot 10-pole and 12-slot 8-pole types, respectively.

SECTION II. Electromagnetic Field Analysis Using CE-FEA

During steady-state operation, the rotor moves synchronously with the rotating air-gap magnetic field, in the presence of stator slots, discrete distribution of the windings, and time harmonics present in the phase current due to the PWM-type supply, which cause a variation in the PM flux density, that can be expressed as follows:

$$B(t) = B_0 + \sum_{\nu} B_\nu \cos(\nu\omega_1 t + \varphi_\nu)$$

(1)

where B_ν and φ_ν are the magnitude and phase angle corresponding to the harmonic of order ν, and B_0 is the dc component. Note that because the aforementioned Fourier series is expressed in terms of the fundamental frequency of the stator current pulsation, i.e., ω_1, the order of the rotor field harmonics can be, in principle, a fractional number as explained later.

The traditional approach for calculating the PM flux density waveform employs a time-consuming transient (TS) FEA with a small time step. The alternative approach proposed in this paper builds upon the CE-FEA, which was previously introduced with particular emphasis on the distribution of the magnetic field in the stators of BLPM machines operated from sine-wave current-regulated drives [9]–[10] [11]. In that case, the CE-FEA can fully exploit both the electric and magnetic symmetries existent at the winding and slot pitch level.

For the rotor field, the periodicity is identified at the pole pitch level, and under the eddy-current-related assumptions specified in the next section, a relatively small number of magnetostatic solutions together with a space-time transformation are employed to “construct” (calculate) the PM flux density waveform, i.e.,

$$B(r, \theta, t) = B\left(r, \theta + k\theta_p, t + \frac{k\theta_p}{\omega_1}\right)$$

(2)

where r is the radial position, and θ is the electrical angular space position of a point within the rotor. Here, θ_p is the electrical pole pitch, and k is an integer. By employing CE-FEA, the computational effort is substantially reduced and the calculation speed increased, as compared with the TS-FEA approach.

In principle, the application of CE-FEA with s magnetostatic solutions for a rotor field domain that includes n_p poles provides

$$n = s \times n_p + 1$$

(3)

points on the rotor flux density waveform. The maximum-order harmonic that can be used for Fourier analysis is determined by the Nyquist theorem. In order to avoid any aliasing effects, this number should be higher than the order of any rotor harmonic that is expected to have a significant magnitude.

SECTION III. Eddy-Current Losses in the PMs

Rare-earth PMs, such as those of the NdFeB type, are electrically conductive, and hence variations of the magnetic-field-produced eddy currents. In order to minimize these currents, a typical engineering approach is to segment the PMs, i.e., to employ multiple individual PM blocks both in the rotor axial direction and in the circumferential direction. The expectation is that the power losses in PMs will be minimized and that the eddy-current effect will be resistance limited, such that it will not change the original magnetic field distribution, which would be present in the machine should there be no eddy currents.

In order to reduce the eddy-current losses, it is also recommended to select the thickness of the PM blocks, i.e., h, to be smaller than the skin depth, corresponding to the highest order field harmonic that is expected to have a significant magnitude. This harmonic is typically generated by the PWM switching frequency, and further details regarding this topic are presented, for example, in [12].

The skin depth for a frequency f can be calculated as

$$\delta = \sqrt{\frac{\rho}{\pi f \mu_0 \mu_r}}.$$

(4)

The following case studies assume a typical constant value for the relative permeability μ_r of 1.05 and PM resistivity ρ of 1.5×10^{-7}m/S, which yields the dependence plotted in Fig. 1 at an operating temperature of 100 °C.

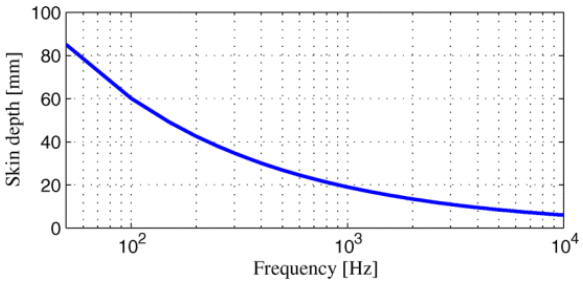

Fig. 1. Variation of skin depth with frequency for a typical NdFeB PM.

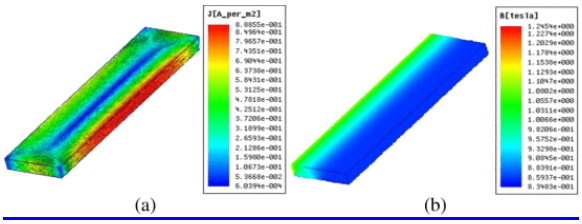

Fig. 2. Example electromagnetic field distribution in a PM calculated by 3-D FEA. (a) Eddy current. (b) Flux density.

The method proposed is based on the assumption that, as it is generally the case in industrial practice, the eddy-current effect is resistance limited through the employment of adequate engineering designed solutions, such as the aforementioned PM segmentation, which could be based on laborious computational methods [7], or more often, on practical experience. Other typical assumptions employed are that the PM material is isotropic and that there is no variation of the electromagnetic field in the axial z-axis direction.

The eddy-current and flux density distributions in a PM are demonstrated in Fig. 2, and the corresponding eddy-current circulating loops are illustrated with dotted lines in Fig. 3. For the initial explanation, assuming that the magnetic field is uniformly distributed in space, a filamentary loop in the $x-z$ plane, which is perpendicular to the PM direction of magnetization, extends along the y-axis direction to the full extent of magnet thickness h.

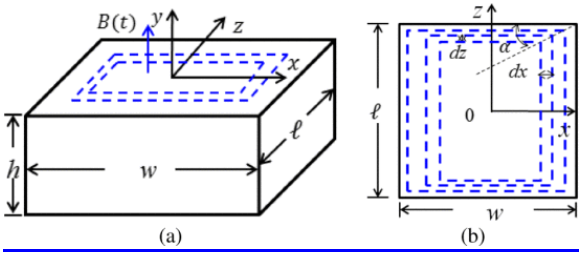

Fig. 3. Schematic eddy-current loops in a rectangular block PM. (a) 3-D view. (b) 2-D view in the x−z plane.

The variable for the axial direction, i.e., z, is not independent and can be expressed as a function of the PM width w, height h, and axial length ℓ and of the x variable, i.e.,

$$z(x) = \frac{\ell}{2} - \left(\frac{w}{2} - x\right) k_z = z_0 + k_z x$$

(5)

where

$$k_z = \tan\alpha, z_0 = \frac{\ell}{2} - \frac{w k_z}{2}.$$

(6)

Here, α is the angle between the straight line connecting the corners of the eddy-current loops, as shown in Fig. 3(b), and the side of these eddy-current loops that is parallel to the x-axis direction, again as depicted in Fig. 3(b).

The magnetic flux through an eddy-current loop is equal to

$$\phi(x,t) = B(t)[2x \cdot 2z(x)] = 4B(t)[z_0 x + k_z x^2].$$

(7)

The induced voltage in the eddy-current circulating loop is calculated from Faraday's law as follows:

$$E(x,t) = -\frac{d\phi(t)}{dt} = -4\frac{dB(t)}{dt}[z_0 x + k_z x^2].$$

(8)

The differential resistance of the eddy-current loop can be estimated using the following expression:

$$dR(x) = \frac{4\big(k_e x + z(x)\big)\rho}{h dx} = \frac{4\rho}{h}\frac{(k_e + k_z)x + z_0}{dx}$$

(9)

where k_e is a coefficient with an original value equal to 1, which can be adjusted to correct for end effects. For example, if the PM is very long in comparison with the width, the angle α can be assumed to be zero, and k_z and k_e are equal to zero. In this case, the end-effect contribution on the resistance is neglected, and the calculation is simplified to

$$dR(x) = \frac{2\ell\rho}{h dx}.$$

(10)

Although this approach for modeling end effects is mostly based on geometry rather than physics, it is very useful as it enables, on one hand, the implementation of a means for calibrating, if necessary, the analytical results against other data provided by experiments or 3-D FEA. On the other hand, when the resistive end effects are neglected, the results can be compared against (quasi) 2-D FEA, which implicitly considers an ideal short circuit at the two axial ends.

The power loss associated with one eddy-current loop having the end effect resistance incorporated through (9) is equal to

$$\frac{E^2(x,t)}{dR(x)} = \left(\frac{dB(t)}{dt}\right)^2 \frac{4\rho}{h}\frac{(z_0 x + k_z x^2)^2}{(k_e + k_z)x + z_0} dx.$$

(11)

Integrating over the entire PM block yields the total eddy-current loss as follows:

$$P_{\mathrm{PM}}(t) = \int_0^{\frac{w}{2}} \left(\frac{dB(t)}{dt}\right)^2 \frac{4\rho}{h} \frac{(z_0 x + k_z x^2)^2}{(k_e + kz)x + z_0} dx$$

$$= \left(\frac{dB(t)}{dt}\right)^2 \frac{4hk_z^2}{\rho(k_e + k_z)} \times \left[\frac{w^4}{64} + \frac{(k_z + 2)z_0 w^3}{24k_z(k_e + kz)} + \frac{z_0^2 w^2}{8k_z^2(k_e + k_z)^2} - \frac{z_0^3 w}{2k_z^2(k_e + kz)^3} + \frac{z_0^4}{k_z^2(k_e + k_z)^4} \ln \frac{w(k_e + k_z) + 2z_0}{2z_0}\right].$$

(12)

In the general case, the spatial distribution of the PM flux density is nonuniform. In principle, in order to increase the accuracy of loss calculation, the magnet block can be discretized in a computational grid with columns along the x-axis and rows along the y-axis. A 4×4 example grid is shown in Fig. 4. The flux density within the grid is denoted by B_{ij}, where i and j are the index for the row and column, respectively. The flux density is still assumed to be constant along the z-axis.

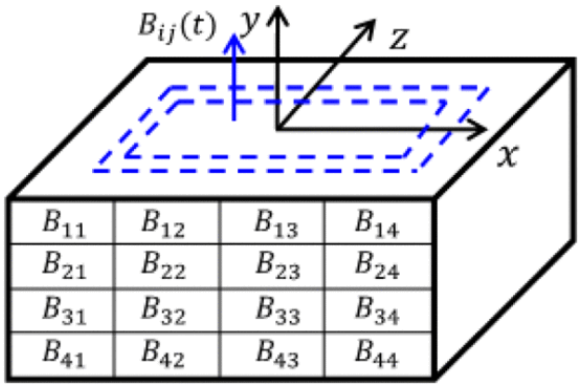

Fig. 4. Example computational grid used for calculating the magnetic flux in a PM. These grids just stand for the sampling points of flux densities in the PM, which does not mean that the magnet is broken into small regions.

The flux linkage and resistance of each eddy-current loop are related to the width of each loop along the x-axis direction, as depicted in Fig. 3. This means that these quantities are functions of the position x, as given in expressions (8) and (9). Thus, the method of utilizing a virtual search coil to measure the flux linkage for the direct calculation of each eddy-current loop voltage is more

cumbersome in comparison to the approach used here. When utilizing this method, the number of virtual search coils will significantly affect the accuracy of the calculation of PM losses. More virtual search coils leads to more accurate results, which also leads to the difficulty of implementing a large number of virtual search coils for all the eddy-current loops. However, in the method implemented in this paper, the discretely sampled flux densities can be used to estimate the flux linkages of all the eddy-current loops at different positions. These flux densities along the x- and y-axis directions are assumed to be uniformly distributed in each block in Fig. 4. In this case, the magnetic flux through a rectangular eddy-current loop is provided by (13), shown at the bottom of the page. These flux linkages are used to derive the voltage of each eddy-current loop related to the position along the x-axis direction.

$$\phi_i(x,t) = \begin{cases} [B_{i2}(t) + B_{i3}(t)]2xz(x), & \text{for} 0 \le |x| \le \frac{w}{4} \\ [B_{i2}(t) + B_{i3}(t)]\frac{wz(x)}{2} + [B_{i1}(t) + B_{i4}(t)]2\left(x - \frac{w}{4}\right)z(x), & \text{for} \frac{w}{4} < |x| \le \frac{w}{2} \end{cases}$$

(13)

The resistance of an eddy-current loop within a layer (row) considering the end effects is given by

$$dR_i(x) = \frac{4\rho(k_e x + z)}{\frac{h}{i}dx} = \frac{4i\rho}{h}\frac{(k_e + k_z)x + z_0}{dx}$$

(14)

and the total eddy-current loss in the PM can be calculated as

$$P_{PM}(t) = \sum_i \int_0^{\frac{w}{2}} \left(\frac{d\phi_i(x,t)}{dt}\right)^2 \frac{h}{4i\rho[(k_e + k_z)x + z_0]}dx\,.$$

(15)

The resistive end effects can be ignored by setting $k_e = 0$ in the previous equation.

While demonstrated in the paper for IPM motors, the method can, in principle, be extended for application to surface-mounted PM machines. Due to the typical nature of the flux density variation in the PMs placed on the surface of the rotor, in this case, it is recommended to employ a large discretization network.

SECTION IV. Case Studies and Discussions

The methods previously presented have been implemented using the ANSYS electromagnetic FEA software [13]. The following example results are provided by two IPM motor designs rated for 10 hp at 1800 r/min. The machines employ fractional-slot concentrated-winding arrangements in the stator and

a conventional rotor topology with one slot per pole. Such IPM designs are prone to relatively high PM losses due to the high harmonic content of the stator field and because of the proximity of the magnets to the air gap. In order to minimize the PM eddy-current losses, various segmentation arrangements with multiple PM blocks per rotor slot were considered, as specified in Table I.

Table I Number of PM Blocks per Pole in Example Segmentation Schemes for a Topology with One Rotor Slot per Pole

Segmentation scheme	SEG1	SEG2	SEG3	SEG4
Axial PM blocks	1	2	1	2
Circumferntial PM blocks	2	2	3	3

As a first step of the analysis, the FEA domain is modeled, and the PMs are discretized for computational purposes in a uniform grid, as shown in Fig. 4. Second, the PM flux density waveforms are calculated with CE-FEA, and the results are analyzed for both harmonic content and spatial variation. Finally, the PM eddy-current losses are calculated and compared with data obtained through 2-D and 3-D TS-FEA.

A. IPM with 12 Slots and 10 Poles

For the 12-slot 10-pole IPM case study, the computational domain corresponding to the general electromagnetic periodicity comprises five poles, as shown in Fig. 5(a). For any point within a PM, a CE-FEA employing seven magnetostatic solutions yields the discrete points shown on a flux density waveform in Figs. 6 and 7. Using the CE-FEA techniques, the waveform corresponding to an entire time cycle is “constructed” (assembled) based on (2) and on the information provided by each individual pole, as illustrated in Fig. 6, through the use of colored coded points and arrows.

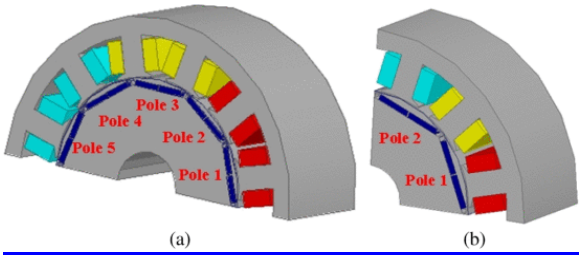

Fig. 5. Geometry of the (a) 12-slot 10-pole and (b) 12-slot 8-pole IPM motor case studies.

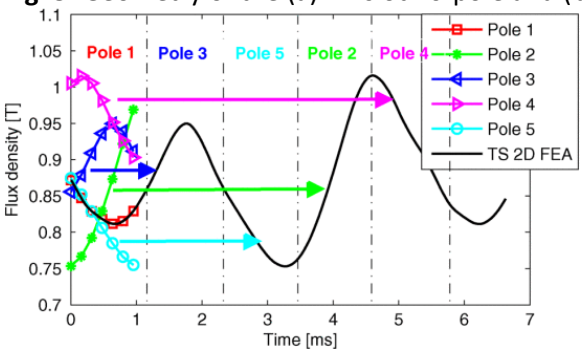

Fig. 6. PM flux density waveform construction according to CE-FEA for the 12-slot 10-pole IPM motor case study.

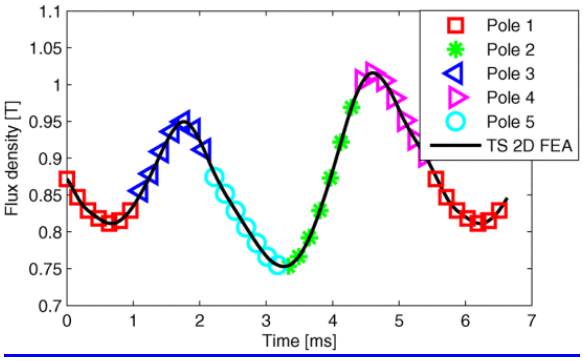

Fig. 7. PM flux density waveform at rated load operation calculated by CE-FEA and TS-FEA.

In this case, there are 35 points on the resultant waveform, meaning that harmonics up to the 15th order can be calculated (see Table II). The CE-FEA calculated waveform virtually overlaps the results obtained with the substantially more computationally expensive conventional TS-FEA (see Fig. 7).

Table II Example Harmonic Spectrum of the Flux Density in the PMs of the 12-Slot 10-Pole IPM

$f_1 = 150Hz$						
Frequency [Hz]	0	180	360	540	720	1080
B[T]	0.870	0.045	0.094	0.003	0.013	0.003

For reference, the PM blocks employed in the SEG1 arrangement have a width of 18.44 mm, a thickness of 4.24 mm, and an axial length of 83.15 mm. Accordingly, in a SEG2 scheme, which uses two PM blocks per rotor length, the ratio of PM axial length per cross-sectional width is 2.257, and consequently, the end effects are expected to be significant.

The spatial distribution of the flux density across the PM cross section was studied using a 4×4 grid, as per Fig. 4. In line with expectations for the considered example, the variation of both the flux density and of its time derivative along the radial direction is small, and more noticeable differences are registered along the circumferential direction (see Fig. 8).

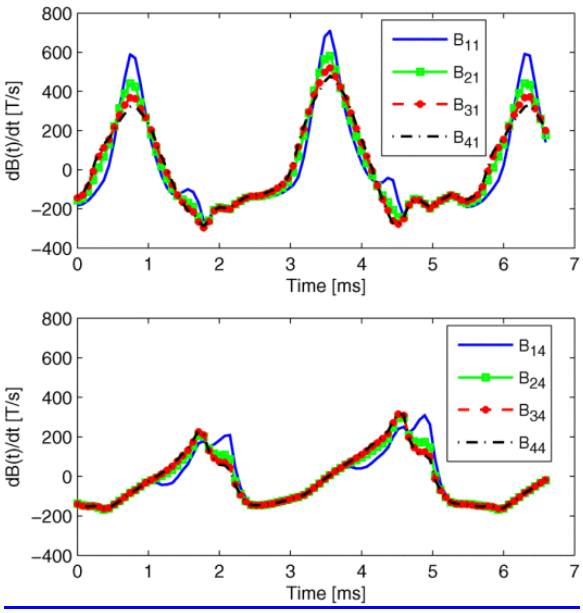

Fig. 8. Waveforms of $\frac{dB(t)}{dt}$ at various points in a PM of the 12-slot 10-pole IPM with the SEG1 segmentation.

To evaluate the capabilities of the eddy-current PM loss calculation method, even in its simpler formulation, only the average value of the flux density was considered for each PM block in conjunction with (12). The rated load results for different PM segmentation schemes are illustrated in Fig. 9 and summarized in Table III. Satisfactory agreement is observed between 3-D FEA and the proposed method with the consideration of the end effects. Further validation is provided through the correlation noted between 2-D FEA and the new method when the resistive end effects are neglected.

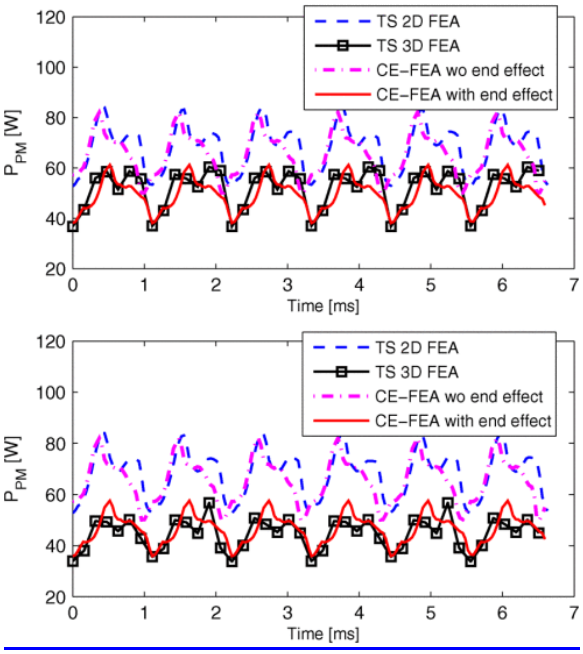

Fig. 9. Time variation of PM losses in the 12-slot 10-pole IPM with SEG1 (top graph) and SEG2 segmentations, respectively.

Table III Average PM Eddy-Current Losses for the 12-Slot 10-Pole IPM

Seg. Type	TS 2D FEA	TS 3D FEA	CE-FEA wo end effect	CE-FEA with end effect
	[W]	[W]	[W]	[W]
SEG1	68.2	51.8	65.5	49.4
SEG2	68.2	44.6	65.5	45.0
SEG3	35.5	28.1	35.0	27.4
SEG4	35.5	26.2	35.0	26.2

B. IPM with 12 Slots and 8 Poles

In the case of the 12-slot 8-pole IPM example, the minimum domain required for the FEA contains only two poles, as shown in Fig. 10, where the square and triangle symbols represent the flux density values across two poles at different rotor positions. Similar to the previous case study, the CE-FEA model made use of seven magnetostatic field solutions. The seven sampling points covering the second pole, namely, pole 2, were space-time transformed to construct the flux density waveform sequentially following the seven points of pole 1, which yielded, in this case, the 15 points covering a waveform of a

full cycle, and the procedure is schematically illustrated in Fig. 10. Again, very good agreement between the flux densities from the CE-FEA and those obtained from the conventional TS-FEA (see the solid line) was reached.

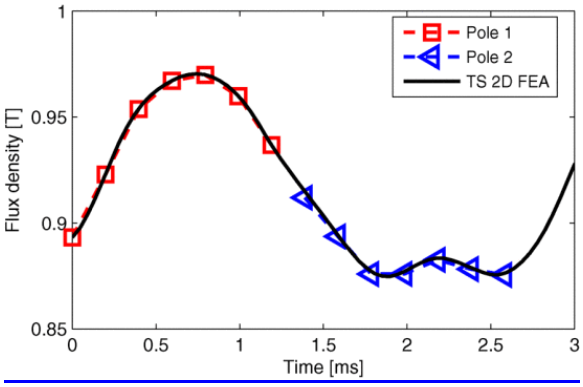

Fig. 10. PM flux density waveform at rated load operation calculated by CE-FEA and TS-FEA.

Using the CE-FEA example waveform data, the rotor field harmonics up to the 15th order were calculated (see Table IV). It should be noted that, according to the theory and numerical results, the fundamental frequency of the rotor flux waveform is different from the fundamental frequency f_1 of the stator MMF and air-gap revolving field. This can be observed for both the previous 12-slot 10-pole IPM case study and the current 12-slot 8-pole IPM example, for which there are three electric cycles of the field inside the PM per each electric cycle of the stator fundamental field.

Table IV Example Harmonic Spectrum of the Flux Density in the PMs of the 12-Slot 8-Pole IPM

$f_s = 120Hz$					
Frequency [Hz]	0	360	720	1080	1440
B[T]	0.916	0.49	0.011	0.005	0.002

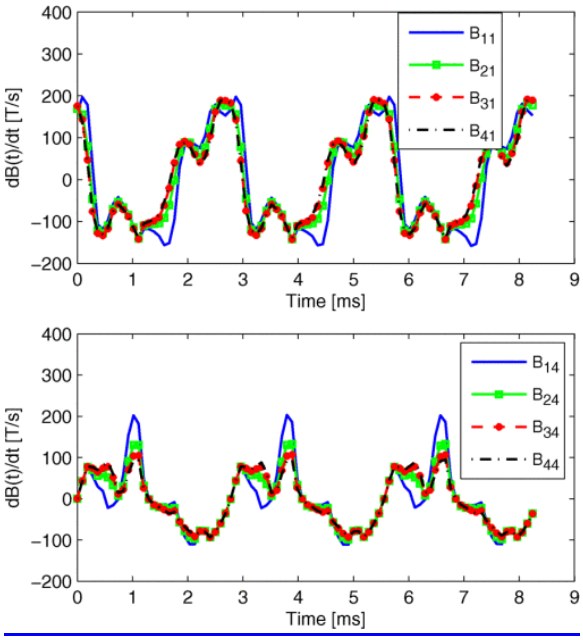

Fig. 11. Waveforms of dB(t)/dt at various points in a PM of the 12-slot 10-pole IPM with the SEG1 segmentation.

The variation of the flux density derivative with respect to time within a 4×4 grid (see Fig. 4) is shown in Fig. 11. As compared with the 12-slot 10-pole IPM design, these variations are smaller, leading to lower losses for comparable PM segmentation arrangements in the 12-slot 8-pole configuration, as demonstrated by the average results summarized in Table V. For reference, the PM blocks employed in the SEG1 arrangement for the 12-slot 8-pole example IPM have a width of 23 mm, a thickness of 4.24mm, and an axial length of 166.3 mm.

Table V Average PM Eddy-Current Losses for the 12-Slot 8-Pole IPM

Seg. Type	TS 2D FEA	TS 3D FEA	CE-FEA wo end effect	CE-FEA with end effect
	[W]	[W]	[W]	[W]
SEG1	33.2	27.6	33.4	26.6
SEG2	33.2	22.3	33.4	23.7
SEG3	15.4	14.1	15.3	13.3
SEG4	15.4	11.6	15.3	12.6

It is interesting to note that, as indicated by the results plotted in Fig. 12 and by the data from Table V, for the 12-slot 8-pole IPM example, as well as for the previous 12-slot 10-pole case study, the most effective means for substantially reducing PM eddy-current losses is the circumferential magnet segmentation. This observation might not be applicable to other types of PM machines, because PM losses would depend on the aspect ratio of the magnet width and axial length in relation to the pole pitch of each of the space harmonics that are causing the losses.

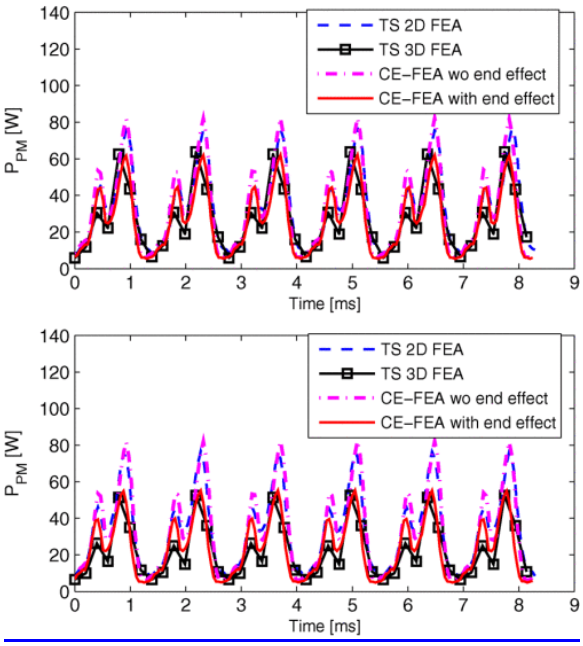

Fig. 12. Time variation of PM losses in the 12-slot 8-pole IPM with SEG1 (top graph) and SEG2 segmentations, respectively.

C. Discussion

Eddy-current PM losses are very important as they can directly impact the heat generation, the rotor temperature, and the motor efficiency. For example, in the worst case scenario, for the 10-hp IPM case studies considered, the PM losses can cause the motor efficiency to drop by 1 point, a value that can be very significant in many applications.

The proposed computational method is sensitive to the effects of circumferential and axial magnet segmentations and is able to calculate with satisfactory precision the PM losses, as demonstrated for both IPM case studies. At the same time, the examples show that the PM losses are dependent on machine topology and that, for the same segmentation scheme, the losses are lower in a 12-slot 8-pole configuration than in a comparable 12-slot 10-pole design.

The CE-FEA based technique incorporates the end effects and the axial segmentation effects, which represents a major improvement over conventional 2-D FEA. At the same time, the results for the case studies are comparable with those of 3-D FEA, while the computational resources are reduced and the speed increased by orders of magnitudes. This major advantage is exemplified in Table VI, which contains data obtained with comparable finite-element meshes and with seven magnetostatic solutions for CE-FEA, 42 time steps per electrical cycle for TS 2-D FEA and with 42 time steps per electrical cycle for TS 3-D FEA. All the simulations were performed on a HP Z800 workstation. Here, in the models of TS 2-D and 3-D FEA, the sine-wave current excitation is implemented instead of the voltage excitation. This current excitation can guarantee that the TS 2-D and 3-D FEA have really short TS profiles.

Table VI Examples of Computational Time for Test Problems

IPM example	CE-FEA	TS 2D FEA	TS 3D FEA
12s 10p SEG1	40 sec	2 min	4 days
12s 8p SEG 2	30 sec	1.5 min	2 days

SECTION V. PWM Switching Losses in the PMs

The effect of the current time harmonics, including those associated with the PWM switching frequency, is not incorporated in the previously described CE-FEA technique. For this purpose, an extension of the method is proposed in this section. Explanations are provided for the generic case, in which the phase current waveform ia contains, apart from the fundamental frequency component, one high-frequency component, i.e.,

$$i_a(t) = I_{1\mathrm{pk}} \cos(\omega_1 t + \varphi_1) + I_{W\mathrm{pk}} \cos(\omega_W t + \varphi_W)$$

(16)

where $I_{1\mathrm{pk}}$ and φ_1 are the fundamental peak current and the initial phase angle, respectively. The peak current of the high-frequency component and its pulsation and initial phase angle are denoted by $I_{W\mathrm{pk}}$, ω_W, and φ_W, respectively.

The algorithm can be, of course, extended to include multiple time harmonics in the current waveform, under the assumption that the contribution of each harmonic to the nonlinear magnetic field is

relatively small, such that superposition can be applied as a generally acceptable engineering approach. In the example shown in Fig. 13, the magnitude of the PWM current component is equal to 20% of the fundamental peak current. The PWM component is modulated on top of the fundamental wave to produce a typical current waveform for BLPM motors supplied from power electronics inverters.

The variation of the flux density in the PM at open-circuit operation is caused by the stator-slotted structure under the influence of the traveling rotor field. Further variation is exhibited on the load, and the difference between the two waveforms, which are calculated by CE-FEA and plotted in Fig. 14, can be used to estimate the flux density in the PM, i.e., B_a, due to the stator armature reaction caused by the fundamental current. Numerically, this PM flux density component can be expressed as a function of a permeance wave Λ and the stator MMF wave F, such that

$$B_a(t) = \Lambda(t) \cdot F(t). \quad (17)$$

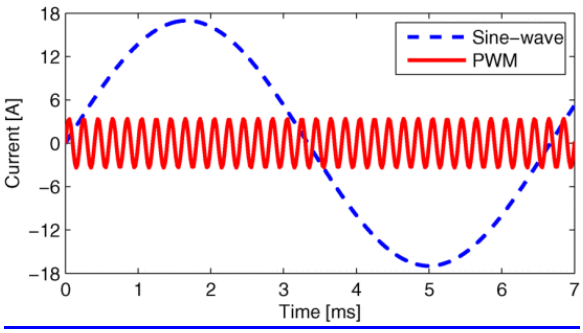

Fig. 13. Fundamental and high-frequency PWM components of the phase current.

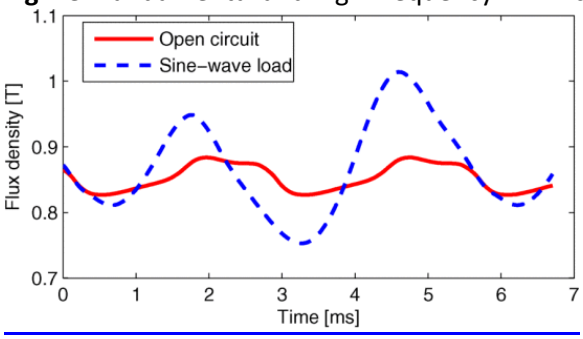

Fig. 14. PM flux densities at open circuit and on load with sine-wave rated current supply.

Further simplification for calculating an equivalent permeance wave can be introduced by neglecting the high-order MMF space harmonics. In this case, only the stator fundamental MMF is present, and this is a standing wave in the rotor reference frame with a time-independent value proportional to the peak fundamental phase current.

The equivalent permeance approach can be also employed for the study of the high-frequency field in the PM and, after superposition with the low-frequency CE-FEA data, can provide satisfactory results. Such an approximated waveform is labeled as harmonic injection and is plotted in Fig. 15 together with the PM flux density computed by the more laborious TS 2-D FEA.

Using the previously described method, calculations were performed for the two IPM motor case studies in the SEG1 arrangement operating at rated load with a PWM switching frequency of 5 and 8 kHz, respectively, and a PWM current ripple, as illustrated in Fig. 13. The results summarized in Fig. 16 indicate satisfactory accuracy for the proposed method, with reasonable agreement between the CE-FEA and TS 2-D FEA obtained results.

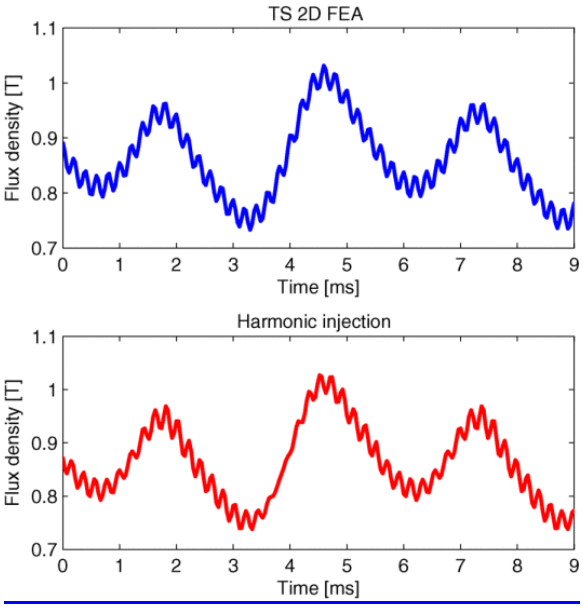

Fig. 15. PM flux density for the example PWM supply from Fig. 13.

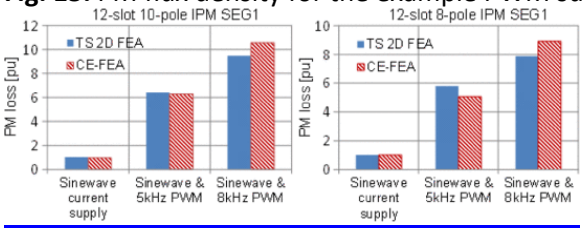

Fig. 16. PM eddy-current losses with PWM switching. Results are expressed in per unit. The TS 2-D FEA with sine-wave current supply was defined as the reference value for each motor.

At the same time, the data are in line with expectations because the PM losses increase with the PWM switching frequency and they can be significant, as compared with losses under pure sine-wave supply. This trend correlates with the reports of other authors, which are based on experimentation and other more laborious 3-D FEA-based methods, e.g., [7].

SECTION VI. Conclusion

The CE-FEA technique described in this paper combines a small number of magnetostatic field solutions with space-time transformations and with a new analytical formulation for calculating PM eddy-current losses. The results provided by two fractional-slot concentrated-winding IPM motor case studies demonstrate satisfactory accuracy and significant decrease in the computational time, as compared with the conventional approaches, which are based on TS-FEA. Based on these advantages, the new method is considered to be particularly suitable for incorporation into large-scale optimal design tools for industrial environments.

Because the proposed power loss calculation method incorporates the 3-D end effects, it can be employed to study the impact of PM block segmentation in the circumferential and axial direction, under the typical assumptions of resistance-limited eddy currents. The sensitivity of the method to PWM switching harmonics was also successfully demonstrated on two example motors.

ACKNOWLEDGMENT

The sponsorship provided by the Regal Beloit Corp. (RBC), NSF-GOALI Grant No: 1028348, and ANSYS Corp. is gratefully acknowledged. Special thanks are due to Mr. Steven Stretz and Mr. Alan Yeadon of RBC and to Dr. Marius Rosu and Mr. Mark Solveson of ANSYS.

References

1. D. M. Ionel, "High-efficiency variable-speed electric motor drive technologies for energy savings in the US residential sector", *Proc. Int. Conf. OPTIM*, pp. 1403-1414, 2010-May.

2. N. A. O. Demerdash and T. Nehl, "Use of numerical analysis of nonlinear eddy current problems by finite elements in the determination of parameters of electrical machines with solid iron rotors", *IEEE Trans. Magn.*, vol. MAG-15, no. 6, pp. 1482-1484, Nov. 1979.

3. F. Deng and T. Nehl, "Analytical modeling of eddy-current losses caused by pulse-width-modulation switching in permanent-magnet brushless direct-current motors", *IEEE Trans. Magn.*, vol. 34, no. 5, pp. 3728-3736, Sep. 1998.

4. Z. Zhu, K. Ng, N. Schofield and D. Howe, "Improved analytical modelling of rotor eddy current loss in brushless machines equipped with surface-mounted permanent magnets", *Proc. Inst. Elect. Eng.—Elect. Power Appl.*, vol. 151, no. 6, pp. 641-650, Nov. 2004.

5. A. Knight and Y. Zhan, "Identification of flux density harmonics and resulting iron losses in induction machines with nonsinusoidal supplies", *IEEE Trans. Magn.*, vol. 44, no. 6, pp. 1562-1565, Jun. 2008.

6. T. Miller, M. McGilp and K. Klontz, "Approximate methods for calculating rotor losses in permanent-magnet brushless machines", *Proc. IEEE IEMDC*, pp. 1-8, 2009-May.

7. K. Yamazaki and A. Abe, "Loss investigation of interior permanent-magnet motors considering carrier harmonics and magnet eddy currents", *IEEE Trans. Ind. Appl.*, vol. 45, no. 2, pp. 659-665, Mar./Apr. 2009.

8. K. Yamazaki and S. Watari, "Loss analysis of permanent-magnet motor considering carrier harmonics of PWM inverter using combination of 2-D and 3-D finite-element method", *IEEE Trans. Magn.*, vol. 41, no. 5, pp. 1980-1983, May 2005.

9. D. M. Ionel and M. Popescu, "Finite-element surrogate model for electric machines with revolving field-application to IPM motors", *IEEE Trans. Ind. Appl.*, vol. 46, no. 6, pp. 2424-2433, Nov./Dec. 2010.

10. D. M. Ionel and M. M. Popescu, "Ultrafast finite-element analysis of brushless PM machines based on space time transformations", *IEEE Trans. Ind. Appl.*, vol. 47, no. 2, pp. 744-753, Mar./Apr. 2011.

11. G. Y. Sizov, D. M. Ionel and N. A. O. Demerdash, "Modeling and parametric design of permanent-magnet ac machines using computationally efficient-finite element analysis", *IEEE Trans. Ind. Electron.*, vol. 59, no. 6, pp. 2403-2413, Jun. 2012.

12. W.-Y. Huang, A. Bettayeb, R. Kaczmarek and J.-C. Vannier, "Optimization of magnet segmentation for reduction of eddy-current losses in permanent magnet synchronous machine", *IEEE Trans. Energy Convers.*, vol. 25, no. 2, pp. 381-387, Jun. 2010.

13. *ANSYS Maxwell*.